

¹ School of Earth and Environmental Sciences, Seoul National University, Seoul, Korea

² Meteorological Research Institute, Korea Meteorological Administration, Seoul, Korea

³ Numerical Weather Prediction Division, Korea Meteorological Administration, Seoul, Korea

Effects of boundary-layer stability on urban heat island-induced circulation

J.-J. Baik¹, Y.-H. Kim², J.-J. Kim³, and J.-Y. Han¹

With 7 Figures

Received February 27, 2006; revised May 3, 2006; accepted May 31, 2006

Published online September 6, 2006 © Springer-Verlag 2006

Summary

The effects of atmospheric boundary-layer stability on urban heat island-induced circulation are numerically and theoretically investigated using a nonlinear numerical model (ARPS) and a two-layer linear analytical model. Numerical model simulations show that as the boundary layer becomes less stable, a downwind updraft cell induced by the urban heat island strengthens. It is also shown that as the boundary layer becomes less stable, both the height of the maximum updraft velocity and the vertical extent of the downwind updraft cell increase. Hence, in the daytime with a nearly neutral or less stable boundary layer the urban heat island-induced circulation can become strong, even though the urban heat island is weak. It is suggested that these findings can be a mechanism for urban-induced thunderstorms observed in the late afternoon or evening with a nearly neutral or less stable boundary layer. The boundary-layer stability affects the spatial distribution of scalar concentration through its influencing urban heat island-induced circulation. Analytical results from a two-layer model with different boundary-layer stabilities in the lower and upper layers are in general qualitatively consistent with the numerical simulation results, although the low-level maximum vertical velocity does not change monotonically with lower-layer stability.

1. Introduction

There are numerous observational studies showing that downwind of urban areas convection and

lightning are more frequent and precipitation tends to be enhanced (e.g. Changnon, 1968; Huff and Changnon, 1972, 1973; Changnon et al., 1991; Shepherd et al., 2002; Diem and Mote, 2005). Possible causes for downwind precipitation enhancement have been proposed. These include increased numbers in cloud condensation nuclei, increased surface roughness, and the urban heat island. An increase in cloud condensation nucleus concentration due to urban air pollution leads to the formation of too many small cloud droplets (e.g. Rosenfeld, 2000), thus suppressing the formation of precipitation-sized drops. There are also studies indicating that urban aerosols may increase precipitation (e.g. Diem and Brown, 2003). Shepherd (2005) summarizes the urban aerosol-precipitation debate. A recent numerical study indicates that increased momentum drag over the city induces convergence on the windward side of the city, but this convergence is not strong enough to initiate moist convection (Rozoff et al., 2003).

A two-dimensional sensitivity study of the development of urban convective precipitation (Thielen et al., 2000) shows that the inclusion of the urban heat island results in increased precipitation over and at a certain distance downwind of the heat island. Their study also shows that

changes in the surface roughness length modify precipitation patterns downwind of the urban surface. In an idealized numerical study of dry and moist convection induced by an urban heat island (Baik et al., 2001), we demonstrated that the urban heat island dynamically induces an organized downwind updraft cell, which can initiate moist convection under favorable thermodynamic conditions. The results from numerical simulations over St. Louis (Rozoff et al., 2003) show the important role of the urban heat island in initiating moist convection downwind of the city.

The stability of the atmospheric boundary layer changes with the time of day. The boundary layer is almost neutral in the daytime in the presence of strong surface heating and turbulent mixing, while it is stable in the nighttime due to longwave radiative cooling. In this paper, we extend our previous work (Baik et al., 2001) and show that the boundary-layer stability is an important factor in determining the intensity of urban heat island-induced circulation. We show this using a two-dimensional numerical model (Sects. 2 and 3) and a two-layer analytical model (Sect. 4).

2. Numerical model and experimental design

The numerical model employed in this study is the Advanced Regional Prediction System (ARPS), which is a compressible, nonhydrostatic, finite difference model with comprehensive physical parameterizations (Xue et al., 1995). To examine the effects of boundary-layer stability on the circulation induced by an urban heat island, dry simulations are performed using a two-dimensional version of the ARPS with surface and radiation processes and Coriolis terms excluded. In addition, a flat surface is assumed and the basic-state horizontal wind (U) is considered to be uniform in the vertical ($U = 3 \text{ m s}^{-1}$ in the present study). These simplifications are made to isolate the effects of boundary-layer stability on urban heat island-induced circulation. Turbulence processes are parameterized using a 1.5-order turbulence closure scheme. The physical domain size is 150 km in the horizontal and 12 km in the vertical. The horizontal and vertical grid intervals are 1 km and 150 m, respectively. To minimize wave reflection at boundaries, a radiation boundary condition is applied to lateral boundaries and a sponge layer is included from $z = 12$ to 15 km.

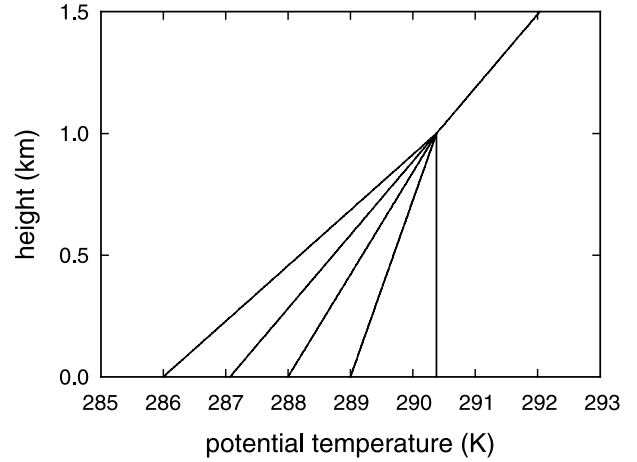


Fig. 1. Vertical profiles of the basic-state potential temperature

The model is integrated for 6 hours with a large time step of 4 s and a small time step of 1 s.

In numerical simulations, the basic-state potential temperature above $z = 1$ km follows that of the standard atmosphere. Below $z = 1$ km, five different profiles of the basic-state potential temperature are considered to examine boundary-layer stability effects (Fig. 1). The potential temperatures at the surface (θ_0) in those five profiles are 286, 287.1, 288, 289, and 290.4 K. The profile of $\theta_0 = 287.1$ K is that of the standard atmosphere. The boundary layer becomes more stable as θ_0 varies from 289 to 286 K. The boundary layer is neutral in the case of $\theta_0 = 290.4$ K. It should be noted that the boundary-layer stability in this study is for the basic state and is regarded as the upwind stratification.

In this study, the urban heat island is represented by adding a thermal forcing term in the thermodynamic energy equation of the ARPS:

$$\rho Q(x, z) = \frac{\rho q_0}{c_p} \frac{a^2}{(x - c)^2 + a^2} e^{-z/h}. \quad (2.1)$$

Here, ρ is the air density, q_0 is the heating amplitude which is regarded as representing the intensity of an urban heat island, c_p is the specific heat of air at constant pressure, a is the half-width of a bell-shaped function, c is the horizontal location of the heating center from the model left boundary, and h is the e -folding height. The specified heating (2.1) decreases horizontally in a bell shape from the heating center and decreases exponentially with height. This heating structure roughly mimics the observed spatial temperature excess

pattern over cities. The parameters a , c , and h are specified as 10 km, 50 km, and 700 m, respectively.

3. Model simulation results and discussion

Figure 2 shows vertical velocity fields at $t = 1$, 3, and 5 h in the case of $\theta_0 = 287.1$ K and $q_0 = 0.8 \text{ J kg}^{-1} \text{ s}^{-1}$. Notice that the center of the specified heat island is located at $x = 50$ km. A heating amplitude of $q_0 = 0.8 \text{ J kg}^{-1} \text{ s}^{-1}$ corresponds to a heating rate of 2.9 K h^{-1} . Considering that the urban heat island is strongest at the heating center and weakens away from the center [see (2.1)], this value of q_0 is reasonable in that a typical maximum difference in the heating/cooling rate between urban and surrounding rural areas under ideal weather conditions is a few degrees per hour (Oke, 1987). The urban heat island induces an updraft cell on its downwind side (Fig. 2). The induced updraft cell moves downwind with an average speed of 1.3 m s^{-1} . This is about half

of the basic-state wind speed ($U = 3 \text{ m s}^{-1}$). The moving updraft cell strengthens its intensity with time, reaches its maximum intensity near $t = 3$ h, and then weakens. The maximum vertical velo-

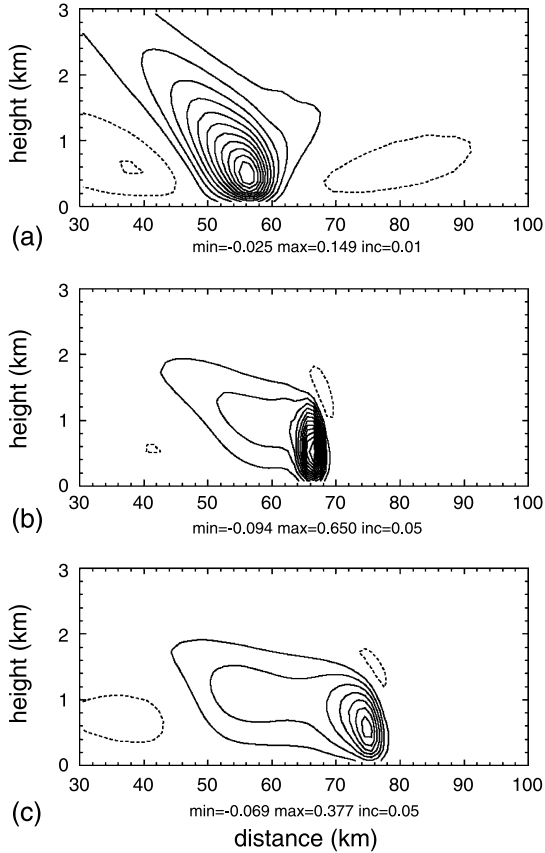


Fig. 2. Vertical velocity fields at $t =$ (a) 1 h, (b) 3 h, and (c) 5 h in the case of $\theta_0 = 287.1$ K and $q_0 = 0.8 \text{ J kg}^{-1} \text{ s}^{-1}$. The solid and dashed lines represent upward and downward motions, respectively, and zero-contour lines are not drawn. The contour interval is 0.01 m s^{-1} in (a) and 0.05 m s^{-1} in (b) and (c).

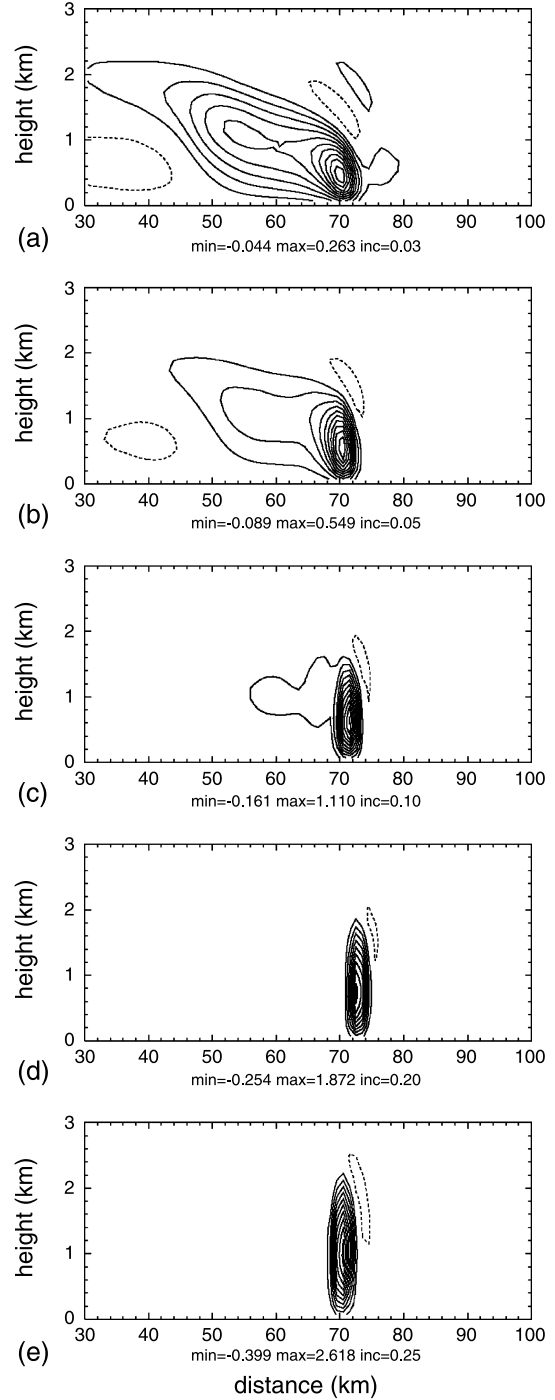


Fig. 3. Vertical velocity fields at $t = 4$ h in the cases of $\theta_0 =$ (a) 286, (b) 287.1, (c) 288, (d) 289, and (e) 290.4 K. In all cases, q_0 is specified as $0.8 \text{ J kg}^{-1} \text{ s}^{-1}$. The contour intervals in (a), (b), (c), (d), and (e) are 0.03, 0.05, 0.1, 0.2, and 0.25 m s^{-1} , respectively.

city in the updraft cell at $t = 3$ h is 0.65 m s^{-1} . Upwind of the urban heat island, a weak downward motion exists. This simulation case belongs to the flow regime revealed when the urban heat island is strong, which is characterized by stationary gravity waves near the heating center and a downwind updraft cell that moves in the downwind direction (Baik et al., 2001). The downwind updraft cell with a peak updraft velocity at low level is essentially nonlinear gravity waves forced by the urban heat island in a stably stratified atmosphere. When the urban heat island is weak, no downwind updraft cell appears.

Figure 3 shows vertical velocity fields at $t = 4$ h simulated with different boundary-layer stabilities (Fig. 1). In all five cases, a downwind updraft cell appears because of the relatively strong urban heat island. As the boundary layer becomes less stable, the maximum vertical velocity in the downwind updraft cell becomes larger. The maximum vertical velocity is largest when the boundary layer is neutral. The maximum vertical velocities in the cases of $\theta_0 = 286, 287.1, 288, 289$, and 290.4 K are $0.26, 0.55, 1.11, 1.87$, and 2.62 m s^{-1} , respectively. It is also observed that as the boundary layer becomes less stable, both the height of the maximum updraft velocity and the vertical extent of the downwind updraft cell increase. Figure 3 clearly indicates that even with the same heating amplitude the intensity of the downwind updraft cell forced by an urban heat island changes significantly depending on boundary-layer stability. The downwind updraft cell forced by an urban heat island can initiate cloud and precipitation when the thermodynamic conditions are favorable for moist convection (Baik et al., 2001). The initiation of cloud and precipitation by the downwind updraft cell should be more probable as the boundary layer becomes less stable.

Two numerical experiments were performed with the same small heating amplitude ($q_0 = 0.2 \text{ J kg}^{-1} \text{ s}^{-1}$) but different boundary-layer stabilities ($\theta_0 = 287.1$ and 290.4 K). No downwind updraft cell appeared in the case of $\theta_0 = 287.1$ K, but a downwind updraft cell did appear in the case of $\theta_0 = 290.4$ K, emphasizing the important role of boundary-layer stability in determining the flow pattern and strength of urban heat island-induced circulation.

It is well known that the urban heat island is more pronounced in the nighttime than in the

daytime (e.g. Oke, 1987). On the other hand, the boundary layer is less stable in the daytime than in the nighttime. In the daytime, the boundary layer can be almost neutral in the presence of strong surface heating and turbulent mixing. Therefore, in the daytime the urban heat island-induced circulation can become strong (a downwind updraft cell can be induced), even though the urban heat island is weak. We suggest that this can be a possible mechanism for urban-induced thunderstorms observed in the late afternoon or evening.

In the above numerical simulations, the heating is specified in the vertical for dynamical simplicity in numerical modeling and theoretical approaches. A more appropriate way might be to add heating only at the lowest one or two model levels, thereby distributing heat vertically by model physics such as turbulence processes. This approach deserves an investigation, especially when the full model-physical processes are activated or a real case is simulated. In addition, since the urban heat island intensity varies with time (e.g. diurnal change), time-dependent heating needs to be included in a future investigation.

To investigate the scalar transport associated with urban heat island-induced circulation under different boundary-layer stabilities, a transport equation for a passive scalar is implemented in the ARPS.

$$\frac{\partial C}{\partial t} + u \frac{\partial C}{\partial x} + w \frac{\partial C}{\partial z} = D_c + S_c, \quad (3.1)$$

where C is the scalar concentration, u and w are the velocity components in the x and z directions, respectively, D_c is the turbulent diffusion term, and S_c is the source/sink term of the scalar. The scalar is released at a rate of 5 ppm s^{-1} at grid points between $x = 45$ and 55 km at the lowest model level ($z = 75$ m).

Figure 4 shows scalar concentration fields at $t = 4$ h in the cases of $\theta_0 = 287.1$ and 290.4 K. In these simulations, q_0 is specified as $0.8 \text{ J kg}^{-1} \text{ s}^{-1}$. In both cases, the maximum scalar concentration is observed at $x = 55$ km at the lowest model level and the horizontal gradient of scalar concentration is large ahead of the downwind updraft cell (Fig. 3b and e) where the flow converges toward the updraft cell. Differences between the two simulations are also obvious. The scalar concentration is lower in the case of $\theta_0 = 290.4$ K (neutral stability case) than in the case of $\theta_0 =$

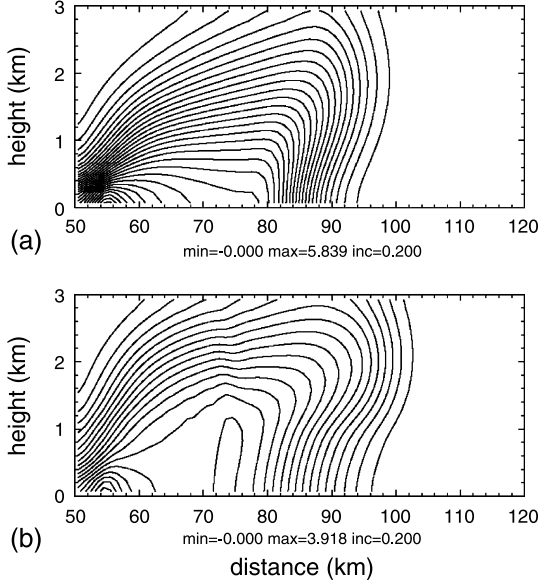


Fig. 4. Scalar concentration fields at $t = 4$ h in the cases of $\theta_0 =$ (a) 287.1 and (b) 290.4 K. In these two cases, q_0 is specified as $0.8 \text{ J kg}^{-1} \text{ s}^{-1}$. The contour interval is 0.2 ppm

287.1 K due to the stronger transport and turbulent diffusion in the case of $\theta_0 = 290.4$ K. A secondary maximum in scalar concentration is observed near $x = 73$ km in the case of $\theta_0 = 290.4$ K. This is attributed to the stronger downwind updraft cell there. These differences indicate that the boundary-layer stability plays an important role in determining the spatial distribution of scalar concentration.

4. A two-layer analytical model

The urban heat island-induced circulation can be theoretically investigated by considering the response of a stably stratified flow to low-level heating (e.g. Olfe and Lee, 1971; Lin and Smith, 1986; Baik, 1992). Along with this line of research, a two-layer analytical model is developed following Chun (1995) to get some insight into the effects of boundary-layer stability on urban heat island-induced circulation. Consider a two-dimensional, steady-state, hydrostatic, nonrotating, inviscid, Boussinesq airflow system. Equations governing small-amplitude perturbations can be written as

$$U \frac{\partial u}{\partial x} = -\frac{\partial \pi}{\partial x}, \quad (4.1)$$

$$\frac{\partial \pi}{\partial z} = b, \quad (4.2)$$

$$\frac{\partial u}{\partial x} + \frac{\partial w}{\partial z} = 0, \quad (4.3)$$

$$U \frac{\partial b}{\partial x} + N^2 w = \frac{g}{c_p T_0} q, \quad (4.4)$$

where u is the perturbation horizontal velocity, w is the perturbation vertical velocity, π is the perturbation kinematic pressure, and b is the perturbation buoyancy, N is the buoyancy frequency, g is the gravitational acceleration, and T_0 is the basic-state temperature. The basic-state horizontal wind $U (> 0)$ is constant and the diabatic heating q is specified as

$$q(x, z) = q_0 \left(\frac{a_1^2}{x^2 + a_1^2} - \frac{a_1 a_2}{x^2 + a_2^2} \right) e^{-z/h}, \quad (4.5)$$

where a_1 and a_2 are constants with $a_1 < a_2$. The widespread cooling term, the second term in parentheses in (4.5), is included to avoid a net heating problem in a linear, steady-state system (Smith and Lin, 1982). Equations (4.1)–(4.4) can be combined to yield a single equation for w , which, after the Fourier transform ($x \rightarrow k$), is given by

$$\frac{\partial^2 \hat{w}}{\partial z^2} + \frac{N^2}{U^2} \hat{w} = \frac{g}{c_p T_0 U^2} \hat{q}. \quad (4.6)$$

Consider a two-layer atmosphere in which the lower layer ($0 \leq z \leq H$, H : boundary-layer depth) has a buoyancy frequency of N_1 and the upper layer ($z > H$) has a buoyancy frequency of N_2 (Fig. 5). General solutions of (4.6) for the lower

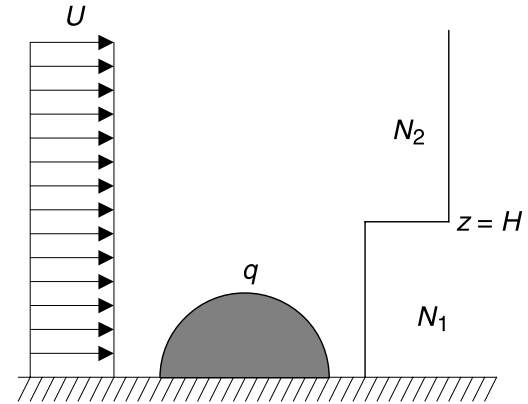


Fig. 5. A sketch of a two-layer analytical model considered in this study. The basic-state horizontal wind U is uniform in the vertical. The lower layer ($0 \leq z \leq H$) has a buoyancy frequency of N_1 and the upper layer ($z > H$) has a buoyancy frequency of N_2 . The concentrated heating region is shaded

(\hat{w}_1) and upper (\hat{w}_2) layers are given by

$$\hat{w}_1(k, z) = A(k)e^{i\lambda_1 z} + B(k)e^{-i\lambda_1 z} + \alpha_1 f(k)e^{-z/h}, \quad (4.7a)$$

$$\hat{w}_2(k, z) = C(k)e^{i\lambda_2(z-H)} + D(k)e^{-i\lambda_2(z-H)} + \alpha_2 f(k)e^{-z/h}, \quad (4.7b)$$

where

$$\lambda_1 = \frac{N_1}{U}, \quad \lambda_2 = \frac{N_2}{U},$$

$$\alpha_1 = \frac{gq_0 h^2}{c_p T_0 U^2 (1 + \lambda_1^2 h^2)},$$

$$\alpha_2 = \frac{gq_0 h^2}{c_p T_0 U^2 (1 + \lambda_2^2 h^2)},$$

$$f(k) = a_1(e^{-a_1|k|} - e^{-a_2|k|}).$$

The coefficients $A(k)$, $B(k)$, $C(k)$, and $D(k)$ in (4.7a) and (4.7b) can be determined by imposing a flat bottom boundary condition ($\hat{w}_1 = 0$ at $z = 0$), upper radiation boundary condition ($D(k) = 0$), and interface conditions at $z = H$ (\hat{w} and $\partial\hat{w}/\partial z$ are continuous at $z = H$). Then, taking the inverse Fourier transform ($k \rightarrow x$) of the solutions in wavenumber space with determined coefficients gives solutions in physical space for the lower (w_1) and upper (w_2) layers.

$$w_1(x, z) = \beta(\alpha_1 - \alpha_2)e^{-H/h} \left[\left(\frac{1}{h\lambda_1} \cos\lambda_1 H - \lambda_{12}^2 \sin\lambda_1 H \right) X_a - \lambda_{12} \left(\cos\lambda_1 H + \frac{1}{h\lambda_1} \sin\lambda_1 H \right) X_b \right] \sin\lambda_1 z - \beta\alpha_1 [X_a \{ \cos\lambda_1 H \cos\lambda_1(z-H) - \lambda_{12}^2 \sin\lambda_1 H \sin\lambda_1(z-H) \} - \lambda_{12} X_b \sin\lambda_1 z] + \alpha_1 X_a e^{-z/h}, \quad (4.8a)$$

$$w_2(x, z) = \beta \left[\left(\frac{1}{h\lambda_1} \sin\lambda_1 H + \cos\lambda_1 H \right) (\alpha_1 - \alpha_2) e^{-H/h} - \alpha_1 \right] [\cos\lambda_1 H \{ X_a \cos\lambda_2(z-H) - X_b \sin\lambda_2(z-H) \} - \lambda_{12} \sin\lambda_1 H \{ X_a \sin\lambda_2(z-H) + X_b \cos\lambda_2(z-H) \}] + \alpha_2 X_a e^{-z/h}, \quad (4.8b)$$

where

$$\beta = \frac{1}{\cos^2\lambda_1 H + \lambda_{12}^2 \sin^2\lambda_1 H},$$

$$\lambda_{12} = \frac{\lambda_2}{\lambda_1},$$

$$X_a = \frac{a_1^2}{x^2 + a_1^2} - \frac{a_1 a_2}{x^2 + a_2^2},$$

$$X_b = a_1 \left(\frac{x}{x^2 + a_1^2} - \frac{x}{x^2 + a_2^2} \right).$$

Using (4.8a) and (4.8b), the vertical profiles of perturbation vertical velocity are plotted in Fig. 6 with $N_1 = 0.0068, 0.0090, 0.0106$, and 0.0122 s^{-1} . These N_1 values are buoyancy frequencies in the boundary layer in the cases of $\theta_0 = 286, 287.1, 288$, and 289 K , respectively (see Fig. 1). The neutral stability case ($N_1 = 0 \text{ s}^{-1}$, $\theta_0 = 290.4 \text{ K}$) is not considered because this case does not support wave-type solutions in the lower atmosphere. The other parameters in all four cases are specified as $q_0 = 0.1 \text{ J kg}^{-1} \text{ s}^{-1}$, $U = 3 \text{ m s}^{-1}$, $N_2 = 0.0106 \text{ s}^{-1}$, $H = 1 \text{ km}$, $h = 700 \text{ m}$, $a_1 = 10 \text{ km}$, $a_2 = 5a_1$, and $T_0 = 0^\circ \text{C}$. The selected loca-

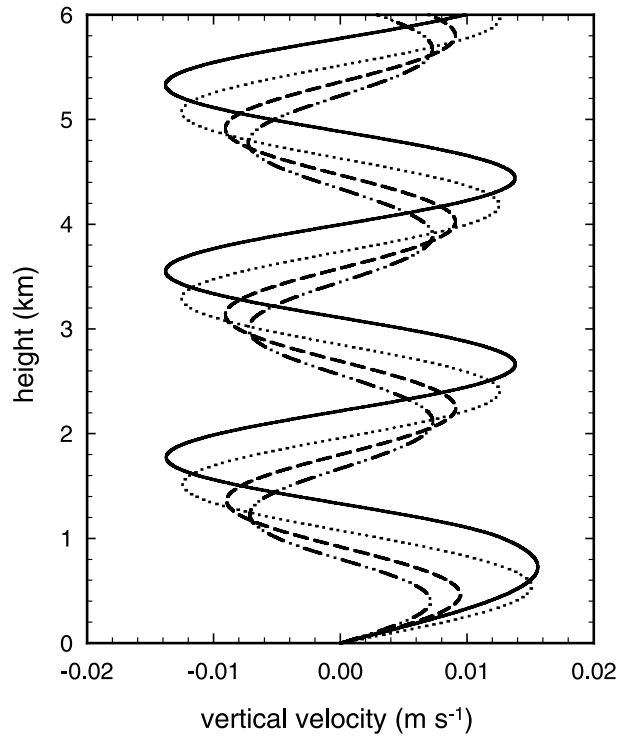


Fig. 6. Vertical profiles of perturbation vertical velocity at $x = 20 \text{ km}$ in the cases of $N_1 = 0.0068$ (solid line), 0.0090 (dotted line), 0.0106 (dashed line), and 0.0122 s^{-1} (dash-dotted line). These are calculated using (4.8a) and (4.8b)

tion is $x = 20$ km, that is, 20 km downwind of the heating center. Since the atmosphere is stably stratified, the response to the heating is internal gravity waves. The vertical wavelength of internal gravity waves in the region of $z > H$ is about 1.8 km. This is the vertical wavelength of station-

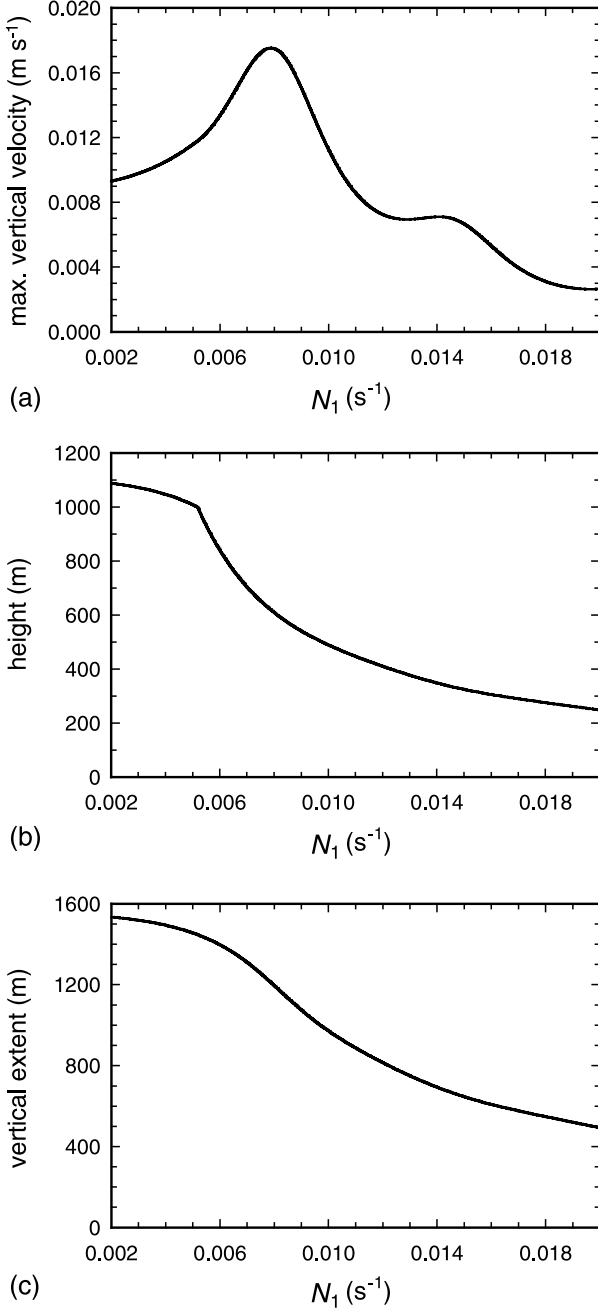


Fig. 7. (a) Low-level maximum perturbation vertical velocity, (b) the height of the low-level maximum perturbation vertical velocity, and (c) the vertical extent of the first upward motion region from the surface as a function of N_1 at $x = 20$ km. These are calculated using (4.8a) and (4.8b)

ary, hydrostatic internal gravity waves $2\pi U/N$. It is seen in Fig. 6 that the wave at this horizontal location amplifies as N_2 decreases from 0.0122 to 0.0068 s^{-1} , that is, as the boundary layer becomes less stable. This result is qualitatively consistent with the numerical modeling result presented in Sect. 3. A close examination of the vertical profiles of perturbation vertical velocity at other downwind locations reveals that the low-level maximum vertical velocity is not always larger in the $N_1 = 0.0068 \text{ s}^{-1}$ case than in the $N_1 = 0.0090 \text{ s}^{-1}$ case. This is related to the fact that the pattern of the low-level maximum vertical velocity with N_1 is not monotonic, as will be shown in Fig. 7.

Figure 6 shows that as the boundary layer becomes less stable, the height at which the maximum vertical velocity at low level appears increases. The height is 0.73, 0.54, 0.46, and 0.40 km in the $N_1 = 0.0068$, 0.0090, 0.0106, and 0.0122 s^{-1} cases, respectively. Figure 6 also shows that as the boundary layer becomes less stable, the vertical extent of the first upward motion region from the surface increases. The vertical extent is 1.33, 1.07, 0.92, and 0.80 km in the $N_1 = 0.0068$, 0.0090, 0.0106, and 0.0122 s^{-1} cases, respectively. These patterns are also observed for other downwind locations away from the concentrated heating region. These results are qualitatively consistent with the numerical modeling results.

The analytical solutions (4.8a) and (4.8b) contain sine and cosine terms, so the patterns of perturbation vertical velocity with stability in the lower layer may not be monotonic for a wider range of N_1 . This possibility is examined with a range of N_1 from 0.002 to 0.02 s^{-1} . Figure 7 shows the low-level maximum perturbation vertical velocity, the height of its location, and the vertical extent of the first upward motion region from the surface as a function of N_1 at $x = 20$ km. The other parameter values specified are the same as those in Fig. 6. There is a prominent peak in the low-level maximum vertical velocity at $N_1 = 0.0079 \text{ s}^{-1}$ (Fig. 7a). In the range of $N_1 = 0.002$ – 0.0079 s^{-1} , the low-level maximum vertical velocity decreases as N_1 decreases. In the range of $N_1 = 0.0079$ – 0.02 s^{-1} , as N_1 decreases from $N_1 = 0.02$ to 0.0079 s^{-1} , the low-level maximum vertical velocity increases gradually, does not change much, and then increases rapidly. However, the other patterns with N_1 are monotonic (Fig. 7b and c). That is, as N_1 decreases,

both the height of the low-level maximum vertical velocity and the vertical extent of the first upward motion region from the surface increases.

The results from a two-layer analytical model (Figs. 6 and 7) indicate that the low-level upward motion downwind of the urban heat island is more pronounced in its magnitude and vertical extent as the boundary layer becomes less stable, although the pattern of the maximum vertical velocity with boundary-layer stability is not monotonic.

5. Conclusion

Recent numerical modeling studies (e.g. Baik et al., 2001) have suggested that the urban heat island plays a crucial role in producing dry convection and initiating moist convection downwind of urban areas. This can be a mechanism for observed precipitation enhancement downwind of urban areas (e.g. Changnon et al., 1991; Shepherd et al., 2002; Diem and Mote, 2005). In this paper, we demonstrated using a nonlinear numerical model (ARPS) and a two-layer linear analytical model that the boundary-layer stability is an important factor that influences the intensity and structure of urban heat island-induced circulation. It was shown that as the boundary layer becomes less stable, a downwind updraft cell induced by the urban heat island strengthens, providing a more favorable environment for initiating moist convection when the thermodynamic conditions are met. The present study indicates that in the daytime with a nearly neutral or less stable boundary layer the urban heat island-induced circulation can become strong, even though the urban heat island is weak. It is suggested that these findings can be a mechanism for urban induced thunderstorms observed in the late afternoon or evening. It is expected that the main results drawn from the two-dimensional nonlinear numerical model simulations and linear analytical calculations would be also valid in three dimensions. An extension to three dimensions is under way.

In this study, we emphasize the roles of the urban heat island and boundary-layer stability in urban-induced or urban-modified weather and climate. It is also known that the rough urban surface can induce or influence circulation and convection (e.g. Thielen et al., 2000). We are investigating the role and relative importance of

the urban surface roughness in urban-induced circulation and convection in comparison with the urban heat island (mechanical vs. thermal) under different boundary-layer stabilities using a three-dimensional dynamical model. In this study, the urban heat island is specified as a steady heat source. A more realistic, time-variant urban heat island could appear in a mesoscale model incorporating sophisticated urban parameterization. Considering that the urban heat island exhibits a diurnal variation, the effects of a time-variant urban heat island on circulation and convection deserve an investigation.

Acknowledgments

The authors thank anonymous reviewers for providing valuable comments on this paper. This work was funded by the Korea Meteorological Administration Research and Development Program under Grant CATER 2006-2202.

References

- Baik JJ (1992) Response of a stably stratified atmosphere to low-level heating – an application to the heat island problem. *J Appl Meteor* 31: 291–303
- Baik JJ, Kim YH, Chun HY (2001) Dry and moist convection forced by an urban heat island. *J Appl Meteor* 40: 1462–1475
- Changnon SA (1968) The La Porte anomaly: fact or fiction? *Bull Amer Meteor Soc* 49: 4–11
- Changnon SA, Shealy RT, Scott RW (1991) Precipitation changes in fall, winter, and spring caused by St. Louis. *J Appl Meteor* 30: 126–134
- Chun HY (1995) Enhanced response of a stably stratified two-layer atmosphere to low-level heating. *J Meteor Soc Japan* 73: 685–696
- Diem JE, Brown DP (2003) Anthropogenic impacts on summer precipitation in central Arizona, U.S.A. *Prof Geogr* 55: 343–355
- Diem JE, Mote TL (2005) Interepothal changes in summer precipitation in the Southeastern United States: evidence of possible urban effects near Atlanta, Georgia. *J Appl Meteor* 44: 717–730
- Huff FA, Changnon SA (1972) Climatological assessment of urban effects on precipitation at St. Louis. *J Appl Meteor* 11: 823–842
- Huff FA, Changnon SA (1973) Precipitation modification by major urban areas. *Bull Amer Meteor Soc* 54: 1220–1232
- Lin YL, Smith RB (1986) Transient dynamics of airflow near a local heat source. *J Atmos Sci* 43: 40–49
- Oke TR (1987) *Boundary Layer Climates*, 2nd edn. Routledge, 435 pp
- Olfe DB, Lee RL (1971) Linearized calculations of urban heat island convection effects. *J Atmos Sci* 28: 1374–1388

- Rosenfeld D (2000) Suppression of rain and snow by urban and industrial air pollution. *Science* 287: 1793–1796
- Rozoff CM, Cotton WR, Adegoke JO (2003) Simulation of St. Louis, Missouri, land use impacts on thunderstorms. *J Appl Meteor* 42: 716–738
- Shepherd JM (2005) A review of current investigations of urban-induced rainfall and recommendations for the future. *Earth Interactions* 9: 1–27
- Shepherd JM, Pierce H, Negri AJ (2002) Rainfall modification by major urban areas: observations from space-borne rain radar on the TRMM satellite. *J Appl Meteor* 41: 689–701
- Smith RB, Lin YL (1982) The addition of heat to a stratified airstream with application to the dynamics of orographic rain. *Quart J Roy Meteor Soc* 108: 353–378
- Thielen J, Wobrock W, Gadian A, Mestayer PG, Creutin JD (2000) The possible influence of urban surfaces on rainfall development: a sensitivity study in 2D in the meso- γ -scale. *Atmos Res* 54: 15–39
- Xue M, Droegemeier KK, Wong V, Shapiro A, Brewster K (1995) ARPS version 4.0 User's Guide. CAPS, University of Oklahoma, 380 pp
- Authors' addresses: Jong-Jin Baik (e-mail: jjbaik@snu.ac.kr) and Ji-Young Han, School of Earth and Environmental Sciences, Seoul National University, Seoul 151-742, Korea; Yeon-Hee Kim, Meteorological Research Institute, Korea Meteorological Administration, Seoul 156-720, Korea; Jae-Jin Kim, Numerical Weather Prediction Division, Korea Meteorological Administration, Seoul 156-720, Korea.